Spatially Resolved Mapping of Oxygen Reduction/Evolution Reaction on Solid-Oxide Fuel Cell Cathodes with Sub-10 nm Resolution

Amit Kumar,[†,*] Donovan Leonard,[†] Stephen Jesse,[†] Francesco Ciucci,[‡] Eugene A. Eliseev,[§] Anna N. Morozovska,[⊥] Michael D. Biegalski,[†] Hans M. Christen,[†] Alexander Tselev,[†] Eva Mutoro,[∥] Ethan J. Crumlin,[∥] Dane Morgan,[#] Yang Shao-Horn,[∥] Albina Borisevich,[†] and Sergei V. Kalinin[†,*]

[†]Oak Ridge National Laboratory, 1 Bethel Valley Road, Oak Ridge, Tennessee 37831, United States, [‡]Department of Mechanical Engineering and Department of Chemical and Biomolecular Engineering, The Hong Kong University of Science and Technology, Clear Water Bay, Kowloon, Hong Kong 00852, People's Republic of China, [§]Institute for Problems of Materials Science, National Academy of Science of Ukraine, 3, Krjijanovskogo Street, Kiev, Ukraine 03412, [⊥]Institute of Semiconductor Physics, National Academy of Science of Ukraine, 41, Pr. Nauki, Kiev, Ukraine 03028, [∥]Department of Mechanical Engineering, Massachusetts Institute of Technology, 77 Massachusetts Avenue, Cambridge, Massachusetts 02139, United States, and [#]Department of Materials Science and Engineering, University of Wisconsin—Madison, Madison, Wisconsin 53706, United States

ABSTRACT Spatial localization of the oxygen reduction/evolution reactions on lanthanum strontium cobaltite (LSCO) surfaces with perovskite and layered perovskite structures is studied at the sub-10 nm level. Comparison between electrochemical strain microscopy (ESM) and structural imaging by scanning transmission electron microscopy (STEM) suggests that small-angle grain boundaries act as regions with enhanced electrochemical activity. The ESM activity is compared across a family of LSCO samples, demonstrating excellent agreement with macroscopic behaviors. This study potentially paves the way for deciphering the mechanisms of electrochemical activity of solids on the level of single extended structural defects such as grain boundaries and dislocations.

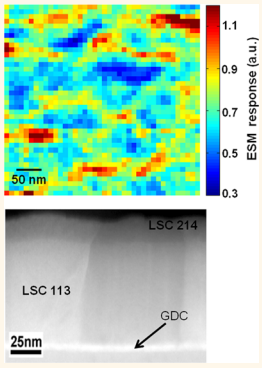

KEYWORDS: electrochemical strain microscopy · fuel cells · cobaltites · electrochemical activity · structural defects

Electrochemical energy conversion systems based on gas—solid interactions such as solid-oxide fuel cells (SOFCs)[1,2] and polymeric electrolyte cells are among the most promising energy technologies, with the efficiency of large-scale SOFC-thermal systems approaching the thermodynamic limit. Similarly, the energy densities of air—metal batteries[3,4] rivaling that of the fossil fuels have attracted much attention to these systems. However, large-scale implementation of these systems is hindered by polarization losses (*e.g.*, 80% of lost efficiency in the hydrogen—oxygen fuel cells is due to cathode polarization)[1,2] and charge—discharge hysteresis (that can achieve 30—40% in Li—air batteries,[5] as compared to several percent in classical intercalation chemistries).[6,7] The traditional solution for activation of gas—solid reactions employs the use of expensive electrocatalysts such as Pt or operation at high temperatures, and the associated costs act as a critical barrier for the broad implementation of fuel cell and metal—air battery technologies.

A breakthrough in the efficiency, lifetimes, and costs of fuel cells and metal—air batteries is possible if fundamental mechanisms underpinning their operation are understood, opening the pathway for knowledge-driven materials and device design.[8] Functionality of these systems is driven by a series of complex mechanisms including oxygen vacancy diffusion, electronic transport, and solid—gas reactions at surfaces and triple phase junctions.[9] Despite the long history of the field,[10] the underpinning mechanisms remain elusive

* Address correspondence to amkum1in@gmail.com; sergei2@ornl.gov.

Received for review July 19, 2012 and accepted April 5, 2013.

Published online April 08, 2013
10.1021/nn303239e

and, despite recent progress,[11] are until now amenable only to macroscopically averaged studies or model experiments using micrometer-scale electrodes.[12−14] At the same time, the structure of solids is generally characterized by the presence of multiple internal interfaces and point and extended defects. The atomic and electronic structure of the defects are now well amenable to advanced electron microscopy techniques,[15] and the defect population can be controlled through synthesis methods.[16] However, the link between (extended) defects and electrochemical reactivity is elusive, limiting the fundamental understanding of gas−solid electrochemical reaction mechanisms and precluding development of predictive atomistic and mesoscopic models.

Here, we study the nature of the electrochemically active state of the SOFC cathode materials with known electrochemical performance using a combination of high-resolution electron microscopy and electrochemical strain microscopy (ESM),[17−19] aiming at achieving nanometer-scale view of the electrochemical reactivity of the surface and correlating it with the nanometer-scale structure and extended structural defects. As a model system, we have chosen the $(La_{0.8}Sr_{0.2})CoO_{3-\delta}$/$(La_{0.5}Sr_{0.5})_2CoO_{4\pm\delta}$ system (LSCO) grown on a yttria-stabilized zirconia (YSZ) substrate with an intermediate Gd-doped CeO_2 buffer layer (GDC). These materials are chosen both as one of the primary electrocatalytic materials with high bulk oxygen diffusion coefficient[10] and due to well-controlled epitaxial growth[19,20] that allows materials with identifiable defect structure to be developed. The use of an ionically conductive and electronically blocking GDC/YSZ electrolyte in conjunction with patterned electrodes allows avoiding electronic transport inevitable at high probing biases and, hence, minimizes artifacts associated with dielectric breakdown.

RESULTS AND DISCUSSION

Here, we explore perovskite surfaces, $(La_{0.8}Sr_{0.2})CoO_{3-\delta}$ (referred to as LSC_{113}, where δ represents the oxygen nonstoichiometry), layered perovskite, $(La_{0.5}Sr_{0.5})_2CoO_{4\pm\delta}$ (referred to as LSC_{214}), and $LSC_{214/113}$ heterostructures of two thicknesses (15 and 0.8 nm thick layers of 214 deposited on 80 nm thick 113 film) designed to improve oxygen reduction reaction (ORR) activity.[20] The ORR functionality of these materials in the form of micropatterned electrodes was extensively studied previously.[20−22] To correlate the high-temperature ORR functionality with room-temperature ESM measurements, electrochemical impedance spectroscopy (EIS) measurements are additionally performed in broad temperature and dc potential ranges (Supporting Information).

Structural Imaging of Defects Using Scanning Transmission Electron Microscopy. To ascertain the structure of the films, identify the primary extended defect types, and determine their structural, electronic, and chemical properties, the material was studied using aberration-corrected scanning transmission electron microscopy (STEM) and electron energy loss spectroscopy (EELS) imaging.[14] To ensure the veracity of direct comparison, the STEM specimens were prepared from the same thin films as were studied by ESM. Note that the STEM measurements were performed prior to the ESM or EIS studies and, hence, do not provide possible information on changes in material microstructure during measurements.

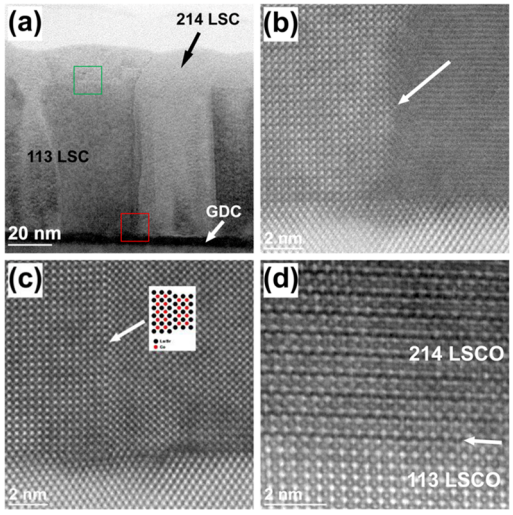

Figure 1. (a) Bright field (BF) STEM micrograph of the LSC214/LSC113/GDC/YSZ heterostructure acquired in the (100) pseudocubic perovskite zone axis orientation. Different types of interfaces are highlighted by boxes. Close-up HAADF STEM micrographs of interfaces: (b) a small angle GB similar to the interface in the red box of panel (a); relative misorientation of the grains is evident in the change of lattice contrast; (c) an antiphase boundary; note exact 90° orientation to the interface; (d) LSC214/LSC113 interface similar to that highlighted by the green box in panel (a).

A bright field micrograph of a $LSC_{214/113}$ film shown in Figure 1a illustrates the presence of columnar grains separated by small angle grain boundaries (GBs), as shown in Figure 1b, and antiphase boundaries (APBs), as shown in Figure 1c. Atomic resolution micrographs of the interface between the ~15 nm LSC_{214} and ~80 nm LSC_{113} layer in Figure 1d show a fully coherent interface between the layers. A similar high degree of coherency is observed between the perovskite LSC_{113} layer and GDC. EELS studies indicate that the GBs and APBs are not associated with measurable cation segregation or significant alteration of electronic structure, presumably due to the very small screening length in LSCO and small interface charges. Similar primary defects are observed for pure LSC_{113} samples. Hence, the well-controlled epitaxial character of systems studied and a small number of possible defect types (GBs, APBs) in combination with the atomically abrupt character of the internal interfaces (LSC_{214}/LSC_{113} and LSC_{113}/GDC) and systematic variation of LSC_{214} layer thickness (none, 0.8 nm, 15 nm, and LSC_{214} only) offer an ideal model system for high-resolution studies.

Spatial Variability of the Electrochemical Behavior Studied Using Electrochemical Strain Microscopy. To explore the

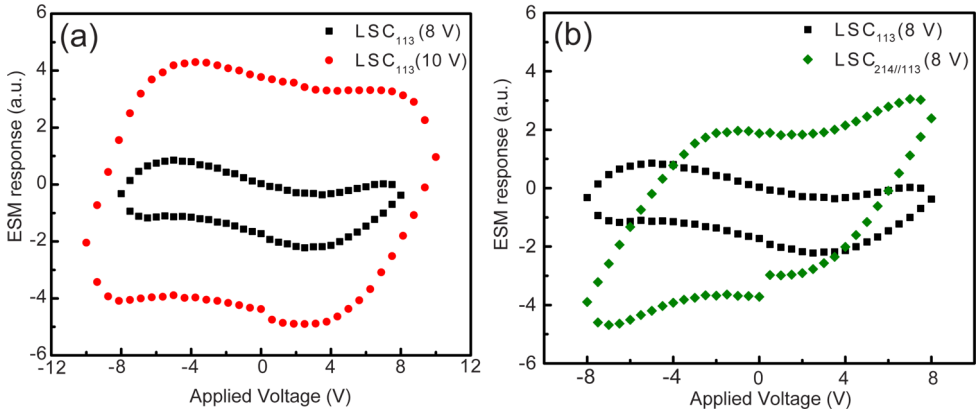

Figure 2. Electrochemical strain microscopy hysteresis loops on LSCO surfaces. (a) ESM data for an LSC_{113} surface for 8 and 10 V bias windows. (b) ESM data for LSC_{113} and $LSC_{214/113}$ surfaces for 8 V bias window. In both cases, 900 hysteresis loops are averaged over a 500 × 500 nm region.

spatial variability of the electrochemical behavior, we employ recently developed electrochemical strain microscopy (ESM).[16−18] In ESM, the biased scanning probe microscopy (SPM) tip is used to apply an electric field to material locally, inducing ionic redistribution and local reversible and irreversible electrochemical processes. The reversible response of material is measured through dynamic electrochemical strain detection, as discussed in detail in ref 23. The onset of irreversible processes can be ascertained by the static surface deformation of the sample surface visible as topographical change after bias pulse application; alternatively, dielectric breakdown can be observed. Here, the spatially resolved measurements were performed in the regime when the irreversible surface deformation was avoided (changes in topography less than ~0.2 nm, below the detection limit of topographic imaging).

The average ESM hysteresis loops are shown in Figure 2. Note that for the LSC_{113} surface the hysteresis loop is closed for the 8 V bias window and opens for the 10 V bias window. A typical bias sweep rate for the measurements is around 16 V/s. In comparison, for the 15 nm $LSC_{214/113}$ surface the hysteresis loop is open at 8 V, suggesting higher ORR activity. Application of higher (by 20−50%) biases for some samples (0.8 nm LSC_{214}) led to irreversible surface deformation clearly visible in topographic images or breakdown. These observations, as well as general considerations on oxide electrochemistry, suggest the following scenario of bias-induced electrochemical processes during ESM measurements. At low biases (below activation of ORR/OER processes on the LSCO surface), field-induced vacancy and electronic motion are possible (polarization at the tip−surface junction), but the total amount of vacancies is preserved. For materials with small (compared to the tip−surface contact area) Debye length as for LSCO, the conservation of vacancy amount combined with the linearity of the Vegard expansion suggests that the hysteretic response will be zero and the ESM hysteresis loop is expected to be closed or have the characteristic elongated shape reminiscent of the minor hysteresis loops in ferroics.[24] Similarly, the hysteresis loop is closed if diffusion times are small compared to the bias sweep times.

Above the critical bias for activation of the ORR/OER process, vacancy injection/annihilation at the surface becomes enabled; that is, the OER process, in Kröger−Vink notation $2O_O^x - 4e^- \rightarrow 2V_O^{\bullet\bullet} + O_2$, for positive biases and the ORR process, $2V_O^{\bullet\bullet} + O_2 + 4e^- \rightarrow 2O_O^x$, becomes active in the tip−surface junction. This process is associated with significant hysteresis due to both slow vacancy motion and ORR/OER activation, and the hysteresis loop adopts a classical shape with well-defined nucleation biases. Note that the critical potentials for this process are determined by both local polarization and electrochemical potential drop in the material and, hence, are larger than for uniform fields. Finally, processes such as vacancy ordering and material amorphization[25] will result in static deformation on a sample surface that can be ascertained by topographic imaging.

The formation of well-defined ESM hysteresis loops allows the spatial variability of the reversible component of the electrochemical process to be studied. Shown in Figure 3 is the ESM mapping of the 15 nm $LSC_{214/113}$ film. Here, the ESM data are acquired in an 8 V bias window over a dense (300 nm) 40 × 40 array, providing spatially resolved information on electrochemical activity. Note the strong variability of the loop area and clearly visible grain-like features. The effective resolution based on this measurement is estimated as ~10 nm, *i.e.*, 3 orders of magnitude below that achievable by classical electrochemical methods.[17]

To get insight into the origin of the observed ESM contrast and separate the electrochemical reaction and transport stages, we analyze the positive/negative bias distribution (PNB and NNB) that can be associated with critical bias for ORR/OER activation in the tip−surface junction.[19] Shown in Figure 3d and e are the maps of the NNB and PNB, respectively, that can be compared with hysteresis loop opening map in

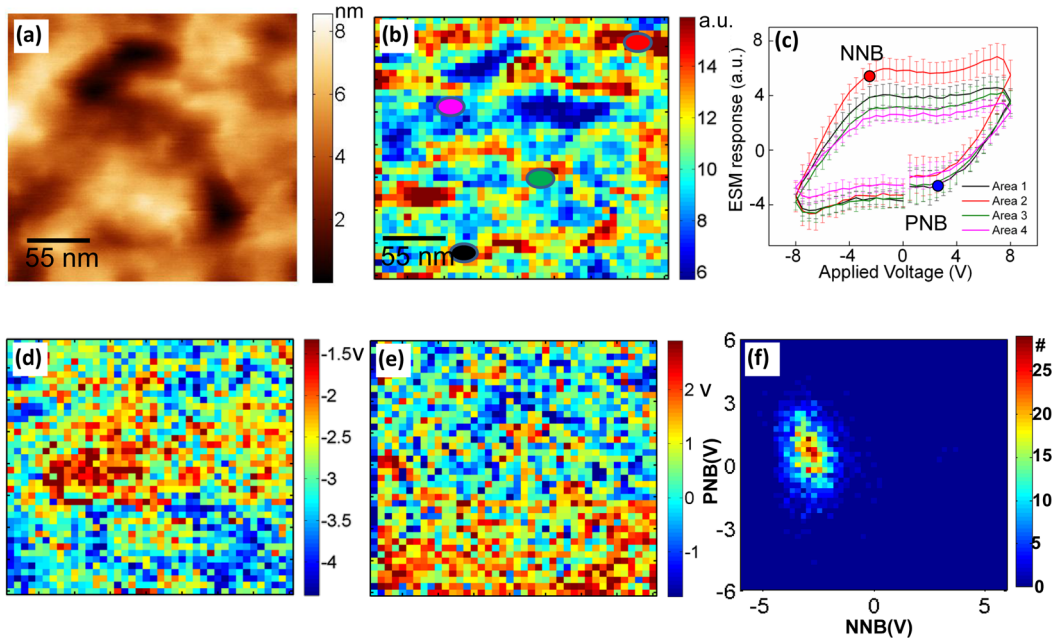

Figure 3. ESM mapping of the 15 nm $LSC_{214/113}$ surface. (a) Surface topography, (b) area under the loop, (c) hysteresis loops from selected locations with color of loops the same as the color of the selected region. Also shown are (d) negative and (e) positive nucleation biases and (f) corresponding 2D histogram of negative and positive nucleation biases.

Figure 3b. Note that the loop area map shows very strong variability well above noise level, whereas PNB and NNB are relatively uniform.

Compared to the 15 and 0.8 nm (not shown) $LSC_{214/113}$ film in Figure 3, studies of the electrochemical reactivity on the crystalline LSC_{113} and LSC_{214} materials are significantly more challenging. While small biases are insufficient for activation of electrochemical processes, the large ones can lead to breakdown precluding the ESM imaging, necessitating multiple measurements. The evolution of surface electrochemical activity for these materials in comparison to microstructure is shown in Figure 4. Note that for the LSC_{113} surface with low ORR activity the grain structure can be barely discerned in the ESM image and significant degradation of contrast with scanning is observed. The LSC_{214} sample shows strong variability of ESM contrast and diffuse grain-like and grain-boundary-like features. This behavior can be correlated with significantly higher disorder in the film, as seen in Figure 4e. Finally, the 15 nm $LSC_{214/113}$ sample combines both the high ORR activity (and hence yields visible ESM contrast) and high localization of signal at the grain boundaries as developed in the LSC_{113} matrix.

The correlation between ESM and electrochemical activity can be further illustrated in the statistical analysis of the PNB and NNB data as compared to the EIS results. Figure 5a illustrates the EIS spectra acquired at 550 °C and corrected for ohmic resistance attributed to oxygen diffusion through the electrolyte. The Nyquist plots can be fit using an equivalent circuit model consisting of an R_{HF}|(parallel R_{MF}, CPE_{MF})|(parallel R_{LF}, CPE_{LF}), where R_{HF} represents the ionic transport through the electrolyte, MF components are proposed to represent the oxygen transport through an interface between electrode and electrolyte, and LF components are responsible for ORR/OER. The R_{HF} is subtracted from the Nyquist plots shown in Figure 5a to more easily compare the dominating LF ORR components.

The corresponding ESM data are illustrated in Figure 5b–d. Here, the mean of the PNB distribution illustrates the distribution of voltages required to induce the OER process $2O_O^x - 4e^- \rightarrow 2V_O^{\bullet\bullet} + O_2$ in the tip–surface junction. The width of the corresponding distribution defines the OER electrochemical disorder. Similarly, the NNB distribution provides the information on the parameters of the ORR process, $2V_O^{\bullet\bullet} + O_2 + 4e^- \rightarrow 2O_O^x$. The value of (PNB − NNB) is a nanoscale analogue of polarization hysteresis. Note that the 0.8 nm $LSC_{214/113}$ sample has the smallest (PNB − NNB) value, indicative of high electrochemical activity, and high disorder. The 15 nm $LSC_{214/113}$ sample has the next smallest (PNB − NNB) value, indicative of high electrochemical activity, and intermediate disorder. The LSC_{214} sample has the third highest activity, but very significant disorder, in excellent agreement with STEM data. Finally, the LSC_{113} sample has very narrow PNB and NNB distributions, but a very high (PNB − NNB) value. This surface is relatively uniform, but the least active of the studied materials. This evolution of electrochemical activity is in excellent agreement with macroscopic behavior, as compared in Figure 5d. Note the excellent correlation between the (PNB − NNB) value and area-specific resistance (note that the least active LSC_{113} film tends to be unstable under ESM imaging conditions). Furthermore,

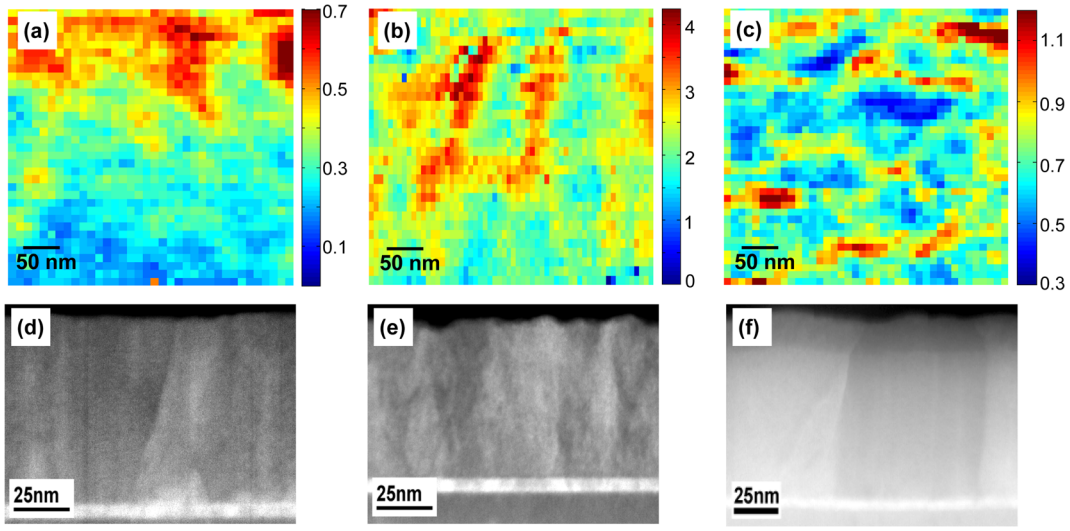

Figure 4. (a–c) Mapping of area under the ESM loop for (a) LSC_{113} thin film, (b) LSC_{214} thin film, and (c) 15 nm $LSC_{214/113}$ thin film. (d–f) HAADF micrographs of the (d) LSC_{113}, (e) LSC_{214} thin film, and (f) 15 nm $LSC_{214/113}$ thin film. STEM and ESM are performed at dissimilar locations on different samples of identical initial composition.

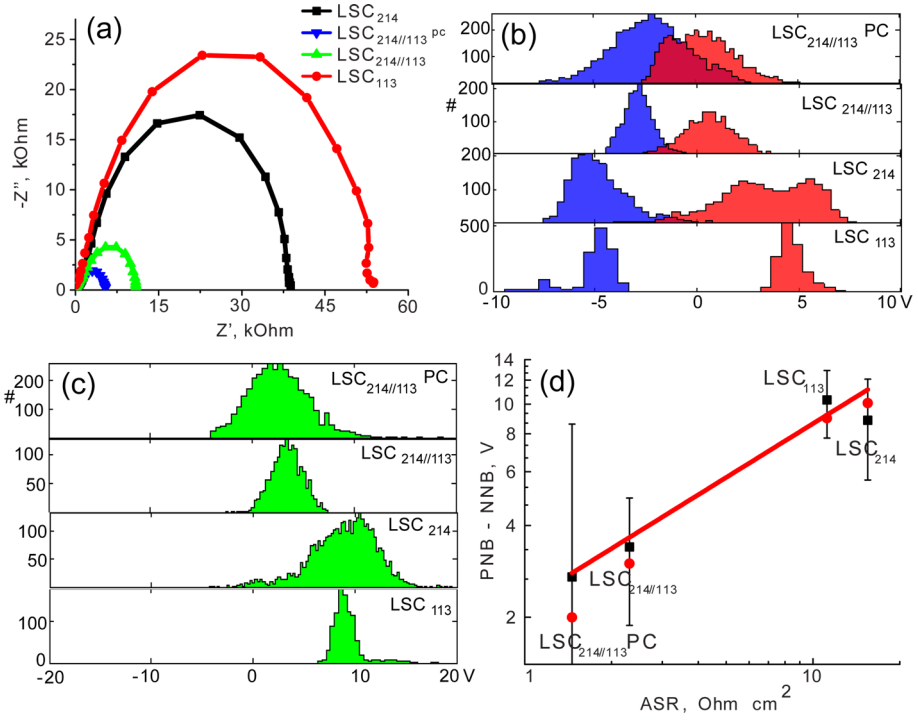

Figure 5. (a) Corrected electrochemical impedance spectra for 0.8 nm $LSC_{214/113}$ thin film, 15 nm $LSC_{214/113}$, LSC_{214}, and LSC_{113} thin films. (b) Histograms of NNB and PNB and (c) histogram of PNB − NNB for the same four samples. (d) Comparison of the area-specific resistance and ESM nucleation biases. Shown are values of PNB − NNB for maxima of histograms (circles) and averages (squares). The error bars correspond to dispersion of distributions in (b, c), *i.e.*, represent the variation in ESM response along the sample surface.

there is a strong correlation between the degree of disorder of the material, as observed in STEM images or inferred as topographic roughness in AFM images, and widths of the ESM potential distributions. This strong correlation between ESM data acquired at room temperature (RT) and EIS parameters at operation conditions for SOFC directly validates the link between ESM data and SOFC-relevant electrochemical functionality. We note that the mechanisms and rate-limiting steps of ORR/OER may be quite different between RT ESM and high-temperature low-bias SOFC operating conditions, for example, due to temperature differences or the presence of a water layer. However, even if this is the case, Figure 5d shows that the ESM data provide a powerful descriptor for SOFC-relevant activity and can therefore be used as a local probe to investigate the latter.

These ESM studies further provide insight into the role of surface modification on ORR activity. The LSC_{214}

layers strongly reduce polarization in ORR/OER processes, but are relatively poor ionic conductors. Correspondingly, ultrathin layers are beneficial for SOFC operation, but increase in the thickness limits the oxygen vacancy transport.

Finally, we briefly discuss the image formation mechanism in ESM in a mixed ionic–electronic conductor (MIEC) as compared to previously studied ionic conductors.[18] For LSCO structures studied here, application of the bias to the SPM tip is expected to bias the whole micropatterned electrode due to the metallic conductivity of LSCO. Hence, in the first approximation the ORR/OER process can be introduced everywhere on the surface. Detailed modeling of the coupled diffusion–migration problem boundary conditions in the static limit illustrates that the vacancy concentration is nearly uniform on the sample surface. However, the SPM tip will be sensitive only to stresses generated in the vicinity of the tip–surface junction. The simple analysis indicates that for very low frequencies ($H < L_D$, where H is the film thickness and L_D is the diffusion/migration length) the resolution is $\sim H$/const with $2 <$ const < 5 (similar to piezoresponse force microscopy on capacitor structures),[26] and for high frequencies the width of the profile will be $\sim L_D$/const. For bulk LSCO, the diffusion and migration length at 300 K for 1 s can be estimated as 8.6×10^{-14} and 4.3×10^{-18} m, respectively. Even given potentially higher diffusion coefficients in the surface layers or in high fields, this rationalizes the extremely high resolution in ESM signals.

CONCLUSIONS

To summarize, using electrochemical strain microscopy we explore the spatial variability of electrochemical reactivity on the LSCO surface with sub-10 nm resolution. In the reversible regime, we demonstrate a strong variability of electrochemical activity along the sample surface on the ~50 nm length scale. Comparison of STEM data suggests that these features correspond to the small-angle grain boundaries within the material. The APBs that has linear geometry are not directly visible on ESM images. The analysis of ESM data suggests that this variability is associated with a distribution of diffusion coefficients, while the critical bias required to activate the ORR/OER process is more uniform. This study hence for the first time reports the electrochemical activity at a single well-defined extended structural defect level.

The nanoscale probing of the electrochemical processes on solid surfaces on a single-defect level will provide a transformative change in the ability to explore and control the mechanisms underpinning ionic systems ranging from fuel cell and metal–air batteries to electroresistive data storage and logic devices. While in the present case we utilize the fact that the defect structure of epitaxial films is dominated by a small number of defect types, this approach can be extended to systems with more complex defect structures. For example, the sequential focused X-ray[27] in combination with ESM measurements or *in situ* (S)TEM-ESM measurements can provide this capability for unknown defects. Overall, the capability to directly link local structure and electrochemical activity will allow the link between atomistic theory and macroscopic electrochemical measurements, and hence knowledge-driven design and optimization of energy storage and conversion systems.

METHODS

Materials. The thin films studied in this work were grown using pulsed laser deposition on a (001) yttria-stabilized zirconia. A thin ~5 nm 20% Gd-doped CeO_2 buffer layer was grown on the YSZ to prevent reaction of lanthanum strontium cobaltite thin films. Growth was performed with a substrate temperature of 450 and 675 °C for the GDC and lanthanum strontium cobaltite thin films with a laser fluence of 1.4 J/cm^2 in a background of 50 mTorr of oxygen. The heterostructures of $(La_{0.5}Sr_{0.5})_2CoO_{4\pm\delta}$ (214) and $La_{0.80}Sr_{0.20}CoO_{3-\delta}$ (113) were also made by growing layers of 214 on top of 113 to obtain $LSC_{214//113}$ films. The films were epitaxial with an epitaxial relationship of $(001)_{YSZ}||(001)_{GDC}||(001)_{LSCO}$ and $(100)_{YSZ}|(100)_{GDC}||(110)_{LSCO}$ assuming a pseudocubic unit cell for LSCO and a cubic unit cell for YSZ and GDC.

Measurements. ESM measurements were performed with a commercial system (Asylum Research Cypher) additionally equipped with a LabView/MatLab-based band excitation controller implemented on a NI-5122/5412 fast AWG and DAQ cards. ESM imaging and spectroscopy were performed with a 200–400 kHz 2 V_{pp} band excitation signal applied to a metal-coated tip. The spectroscopic measurements were performed at ~1 s/pixel waveform with 2 ms at each dc voltage step. Mapping of the electromechanical response was done typically on a 40×40 point grid with a spacing of 20 nm, although other spacing and image sizes were also used. All measurements were performed with the biased tip in direct contact with the sample surface in ambient air and without any additional protective coating. STEM studies were performed using the Titan S 80–300 operated at 300 kV and equipped with CEOS DCOR aberration corrector (Figure 1a–c, Figure 4d–f) and Nion UltraSTEM 60–100 operated at 100 kV and equipped with 5th order quadrupole-octupole aberration corrector (Figure 1d).

Conflict of Interest: The authors declare no competing financial interest.

Acknowledgment. The work was supported (A.K., D.L., A.B.) by the Materials Science and Engineering Division of the U.S. DOE. This research was conducted in part (A.K., S.V.K., M.B.) at the Center for Nanophase Materials Sciences, and as a user project at ShaRE user facility (A.B., D.L.), which are both sponsored at Oak Ridge National Laboratory by the Scientific User Facilities Division, U.S. Department of Energy. The MIT group (Y.S.H., E.C., E.M.) acknowledges the U.S. DOE (SISGR DESC0002633). E.M. is grateful for financial support from the German Research Foundation (DFG research scholarship). F.C. thanks Prof. Wei Lai (Michigan State University) for valuable discussions and acknowledges startup funds from the Hong Kong University of Science and Technology.

Supporting Information Available: Details on the growth of materials used in this work, implementation of electrochemical

strain microscopy, and temperature-dependent electrochemical impedance measurements. This material is available free of charge *via* the Internet at http://pubs.acs.org.

REFERENCES AND NOTES

1. Bagotsky, V. S. *Fuel Cells: Problems and Solutions*; Wiley: New York, 2009.
2. O'Hayre, R.; Cha, S. W.; Colella, W.; Prinz, F. B. *Fuel Cell Fundamentals*; Wiley: New York, 2009.
3. Abraham, K. M.; Jiang, Z. A Polymer Electrolyte-Based Rechargeable Lithium/Oxygen Battery. *J. Electrochem. Soc.* **1996**, *143*, 1–5.
4. Wang, D. Y.; Xiao, J.; Xu, W.; Zhang, J. G. High Capacity Pouch-Type Li-Air Batteries. *J. Electrochem. Soc.* **2010**, *157*, A760–A764.
5. Debart, A.; Paterson, A. J.; Bao, J.; Bruce, P. G. α-MnO_2 Nanowires: A Catalyst for the O_2 Electrode in Rechargeable Lithium Batteries. *Angew. Chem., Int. Ed.* **2008**, *47*, 4521–4524.
6. Huggins, R. A. *Advanced Batteries: Materials Science Aspects*; Springer: New York, 2008.
7. Dreyer, W.; Jamnik, J.; Guhlke, C.; Huth, R.; Moskon, J.; Gaberscek, M. The Thermodynamic Origin of Hysteresis in Insertion Batteries. *Nat. Mater.* **2010**, *9*, 448–453.
8. DOE Basic Research Needs for Electrical Energy Storage. www.er.doe.gov/bes/reports/files/EES_rpt.pdf.
9. Wilson, J. R.; Kobsiriphat, W.; Mendoza, R.; Chen, H. Y.; Hiller, J. M.; Miller, D. J.; Thornton, K.; Voorhees, P. W.; Adler, S. B.; Barnett, S. A. Three-Dimensional Reconstruction of a Solid-Oxide Fuel-Cell Anode. *Nat. Mater.* **2006**, *5*, 541–544.
10. Adler, S. B. Factors Governing Oxygen Reduction in Solid Oxide Fuel Cell Cathodes. *Chem. Rev.* **2004**, *104*, 4791–4843.
11. Louie, M. W.; Hightower, A.; Haile, S. M. Nanoscale Electrodes by Conducting Atomic Force Microscopy: Oxygen Reduction Kinetics at the Pt|$CsHSO_4$ Interface. *ACS Nano* **2010**, *4*, 2811–2821.
12. La O', G. J.; In, H. J.; Crumlin, E.; Barbastathis, G.; Shao-Horn, Y. Recent Advances in Microdevices for Electrochemical Energy Conversion and Storage. *Int. J. Energy Res.* **2007**, *31*, 548–575.
13. Fleig, J. Microelectrodes in Solid State Ionics. *Solid State Ionics* **2003**, *161*, 279–289.
14. Opitz, A. K.; Fleig, J. Investigation of O_2 Reduction on Pt/YSZ by Means of Thin Film Microelectrodes: The Geometry Dependence of the Electrode Impedance. *Solid State Ionics* **2010**, *181*, 684–693.
15. Pennycook, S. J.; Nellist, P. D. *Scanning Transmission Electron Microscopy: Imaging and Analysis*; Springer: New York, 2011.
16. Tuller, H. L.; Bishop, S. R. Tailoring Material Properties through Defect Engineering. *Chem. Lett.* **2010**, *39*, 1226–1231.
17. Balke, N.; Jesse, S.; Morozovska, A. N.; Eliseev, E.; Chung, D. W.; Kim, Y.; Adamczyk, L.; Garcia, R. E.; Dudney, N.; Kalinin, S. V. Nanoscale Mapping of Ion Diffusion in a Lithium-ion Battery Cathode. *Nat. Nanotechnol.* **2010**, *5*, 749–754.
18. Balke, N.; Jesse, S.; Kim, Y.; Adamczyk, L.; Tselev, A.; Ivanov, I. N.; Dudney, N. J.; Kalinin, S. V. Real Space Mapping of Li-Ion Transport in Amorphous Si Anodes with Nanometer Resolution. *Nano Lett.* **2010**, *10*, 3420–3425.
19. Kumar, A.; Ciucci, F.; Morozovska, A. N.; Kalinin, S. V.; Jesse, S. Measuring Oxygen Reduction/Evolution Reactions on the Nanoscale. *Nat. Chem.* **2011**, *3*, 707–713.
20. Crumlin, E. J.; Mutoro, E.; Ahn, S. J.; la O', G. J.; Leonard, D. N.; Borisevich, A.; Biegalski, M. D.; Christen, H. M.; Shao-Horn, Y. Oxygen Reduction Kinetics Enhancement on a Heterostructured Oxide Surface for Solid Oxide Fuel Cells. *J. Phys. Chem. Lett.* **2010**, *1*, 3149–3155.
21. La O', G. J.; Ahn, S. J.; Crumlin, E.; Orikasa, Y.; Biegalski, M. D.; Christen, H. M.; Shao-Horn, Y. Catalytic Activity Enhancement for Oxygen Reduction on Epitaxial Perovskite Thin Films for Solid-Oxide Fuel Cells. *Angew. Chem., Int. Ed.* **2010**, *49*, 5344–5347.
22. Mutoro, E.; Crumlin, E. J.; Biegalski, M. D.; Christen, H. M.; Shao-Horn, Y. Enhanced Oxygen Reduction Activity on Surface-Decorated Perovskite Thin Films for Solid Oxide Fuel Cells. *Energy Environ. Sci.* **2011**, *4*, 3689–3696.
23. Morozovska, A. N.; Eliseev, E. A.; Balke, N.; Kalinin, S. V. Local Probing of Ionic Diffusion by Electrochemical Strain Microscopy: Spatial Resolution and Signal Formation Mechanisms. *J. Appl. Phys.* **2010**, *108*, 053712.
24. Tagantsev, A. K.; Cross, L. E.; Fousek, J. *Domains in Ferroic Crystals and Thin Films*; Springer: New York, 2010.
25. Kubicek, M.; Limbeck, A.; Fromling, T.; Hutter, H.; Fleig, J. Relationship between Cation Segregation and the Electrochemical Oxygen Reduction Kinetics of $La_{0.6}Sr_{0.4}CoO_{3-\delta}$ Thin Film Electrodes. *J. Electrochem. Soc.* **2011**, *158*, B727–B734.
26. Kalinin, S. V.; Rodriguez, B. J.; Kim, S. H.; Hong, S. K.; Gruverman, A.; Eliseev, E. A. Imaging Mechanism of Piezoresponse Force Microscopy in Capacitor Structures. *Appl. Phys. Lett.* **2008**, *92*, 152906.
27. Budai, J. D.; Yang, M.; Larson, B. C.; Tischler, J. Z.; Liu, W.; Ice, G. E. 2D and 3D X-Ray Structural Microscopy Using Submicron-Resolution Laue Microdiffraction. *MRS Proc.* **2004**, *840*, Q7.1.1–Q7.1.6.